Monthly Notices
of the
ROYAL ASTRONOMICAL SOCIETY

MNRAS **450,** 1503–1513 (2015) doi:10.1093/mnras/stv712

Gap formation and stability in non-isothermal protoplanetary discs

Robert Les[1]★ and Min-Kai Lin[1,2]★

[1]*Canadian Institute for Theoretical Astrophysics, 60 St. George Street, Toronto, ON M5S 3H8, Canada*
[2]*Department of Astronomy and Steward Observatory, University of Arizona, 933 North Cherry Avenue, Tucson, AZ 85721, USA*

Accepted 2015 March 27. Received 2015 March 26; in original form 2014 December 22

ABSTRACT

Several observations of transition discs show lopsided dust distributions. A potential explanation is the formation of a large-scale vortex acting as a dust-trap at the edge of a gap opened by a giant planet. Numerical models of gap-edge vortices have so far employed locally isothermal discs in which the temperature profile is held fixed, but the theory of this vortex-forming or 'Rossby wave' instability was originally developed for adiabatic discs. We generalize the study of planetary gap stability to non-isothermal discs using customized numerical simulations of disc–planet systems where the planet opens an unstable gap. We include in the energy equation a simple cooling function with cooling time-scale $t_c = \beta\Omega_k^{-1}$, where Ω_k is the Keplerian frequency, and examine the effect of β on the stability of gap edges and vortex lifetimes. We find increasing β lowers the growth rate of non-axisymmetric perturbations, and the dominant azimuthal wavenumber m decreases. We find a quasi-steady state consisting of one large-scale, overdense vortex circulating the outer gap edge, typically lasting $O(10^3)$ orbits. We find vortex lifetimes generally increase with the cooling time-scale t_c up to an optimal value of $t_c \sim 10$ orbits, beyond which vortex lifetimes decrease. This non-monotonic dependence is qualitatively consistent with recent studies using strictly isothermal discs that vary the disc aspect ratio. The lifetime and observability of gap-edge vortices in protoplanetary discs is therefore dependent on disc thermodynamics.

Key words: accretion, accretion discs – hydrodynamics – instabilities – methods: numerical – planet–disc interactions – protoplanetary discs.

1 INTRODUCTION

The interaction between planets and protoplanetary discs plays an important role in the theory of planet formation and disc evolution. Disc–planet interaction may lead to the orbital migration of protoplanets and modify the structure of protoplanetary discs (see Baruteau & Masset 2013, for a recent review).

A sufficiently massive planet can open a gap in a gaseous protoplanetary disc (Papaloizou & Lin 1984; Bryden et al. 1999; Crida, Morbidelli & Masset 2006; Fung, Shi & Chiang 2014), while low-mass planets may also open gaps if the disc viscosity is small enough (Li et al. 2009; Dong, Rafikov & Stone 2011; Duffell & MacFadyen 2013). Support for such disc–planet interaction have begun to emerge in observations of circumstellar discs that reveal annular gaps (e.g. Debes et al. 2013; Quanz et al. 2013b; Osorio et al. 2014), with possible evidence of companions within them (e.g. Quanz et al. 2013a; Reggiani et al. 2014).

A recent theoretical development in the study of planetary gaps is their stability. When the disc viscosity is low and/or the planet mass is large, the presence of potential vorticity (PV, the ratio of vorticity to surface density) extrema can render planetary gaps dynamically unstable due to what is now referred to as the 'Rossby wave instability' (RWI; Lovelace et al. 1999; Li et al. 2000). This eventually leads to vortex formation (Li et al. 2001, 2005; Koller, Li & Lin 2003; de Val-Borro et al. 2007), which can significantly affect orbital migration of the planet (Ou et al. 2007; Li et al. 2009; Lin & Papaloizou 2010; Yu et al. 2010).

Vortex formation at gap edges may also have observable consequences. Because disc vortices represent pressure maxima, they are able to collect dust particles (Barge & Sommeria 1995; Inaba & Barge 2006; Lyra & Lin 2013). Dust trapping at gap-edge vortices have thus been suggested to explain asymmetric dust distributions observed in several transition discs (e.g. Casassus et al. 2013; Fukagawa et al. 2013; Isella et al. 2013; van der Marel et al. 2013; Pérez et al. 2014; Pinilla et al. 2015).

However, studies of Rossby vortices at planetary gap edges have adopted locally isothermal discs, where the disc temperature is a fixed function of position only (e.g. Lyra et al. 2009; Lin & Papaloizou 2011; Fu et al. 2014; Zhu et al. 2014). On the other hand, the theory of the RWI was in fact developed for adiabatic discs (Li et al. 2000), which permits heating. In adiabatic discs, the

★ E-mail: robert.les@mail.utoronto.ca (RL); minkailin@email.arizona.edu (M-KL)

relevant quantity for stability becomes a generalization of the PV that accounts for entropy variations (Lovelace et al. 1999).

Gap opening is associated with planet-induced spiral shocks. In an isothermal disc, PV-generation across these isothermal shocks leads to the RWI (Koller et al. 2003; Li et al. 2005; de Val-Borro et al. 2007; Lin & Papaloizou 2010). However, if cooling is inefficient and the shock is non-isothermal, then shock-heating may affect gap stability, since the relevant quantity is an entropy-modified PV (described below), and there is entropy generation across the shocks.

For example, previous linear simulations of the RWI found that increasing the sound speed favours instability (Li et al. 2000; Lin 2013). In the context of planetary gaps, however, the increased temperature may also act to stabilize the disc by making gap opening more difficult. It is therefore of theoretical interest to clarify the effect of heating and cooling on the stability of planetary gaps.

In this work, we extend the study of planetary gap stability against vortex formation to non-isothermal discs. We include in the fluid energy equation a one-parameter cooling prescription that allows us to probe disc thermodynamics ranging from nearly isothermal to nearly adiabatic.

This paper is organized as follows. In Section 2, we describe the equations governing the disc–planet system and initial conditions. Our numerical approach, including diagnostic measures, is given in Section 3. We present results from two sets of numerical experiments. In Section 4, we use disc–planet interaction to set up discs with gaps, but study their stability without further influence from the planet. We then perform long-term disc–planet simulations to examine the lifetime of gap-edge vortices in Section 5, as a function of the imposed cooling rate. We conclude and summarize in Section 6 with a discussion of important caveats.

2 DISC–PLANET MODELS

The system is a two-dimensional (2D) non-self-gravitating gas disc orbiting a central star of mass M_*. We adopt cylindrical coordinates (r, ϕ, z) centred on the star. The frame is non-rotating. Computational units are such that $G = M_* = \mathcal{R} = \mu = 1$, where G is the gravitational constant, $\mathcal{R}$ is the gas constant and μ is the mean molecular weight.

The disc evolution is governed by the standard fluid equations

$$\frac{\partial \Sigma}{\partial t} + \nabla \cdot (\Sigma \boldsymbol{v}) = 0, \tag{1}$$

$$\frac{\partial \boldsymbol{v}}{\partial t} + \boldsymbol{v} \cdot \nabla \boldsymbol{v} = -\frac{1}{\sigma} \nabla p - \nabla \Phi + \boldsymbol{f}_\nu, \tag{2}$$

$$\frac{\partial e}{\partial t} + \nabla \cdot (e \boldsymbol{v}) = -p \nabla \cdot \boldsymbol{v} + \mathcal{H} - \mathcal{C}, \tag{3}$$

where Σ is the surface density, $\boldsymbol{v} = (v_r, v_\phi)$ the fluid velocity, p is the vertically integrated pressure, $e = p/(\gamma - 1)$ is the energy per unit area and the adiabatic index $\gamma = 1.4$ is assumed constant.

The total potential Φ includes the stellar potential, planet potential (described below) and indirect potentials to account for the non-inertial reference frame. In the momentum equations, $\boldsymbol{f}_\nu$ represent viscous forces, which includes artificial bulk viscosity to handle shocks, and a Navier–Stokes viscosity whose magnitude is characterized by a constant kinematic viscosity parameter ν. However, we will be considering effectively inviscid discs by adopting small values of ν.

2.1 Heating and cooling

In the energy equation, the heating term $\mathcal{H}$ is defined as

$$\mathcal{H} \equiv Q^+ - Q_i^+ \frac{\Sigma}{\Sigma_i}, \tag{4}$$

where Q^+ represents viscous heating (from both physical and artificial viscosity) and subscript i denotes evaluation at $t = 0$. The cooling term $\mathcal{C}$ is defined as

$$\mathcal{C} \equiv \frac{1}{t_c} \left(e - e_i \frac{\Sigma}{\Sigma_i} \right), \tag{5}$$

where $t_c = \beta \Omega_k^{-1}$ is the cooling time, $\Omega_k = \sqrt{GM/r^3}$ is the Keplerian frequency and β is an input parameter. This cooling prescription allows one to explore the full range of thermodynamic response of the disc in a systematic way: $\beta \ll 1$ is a locally isothermal disc while $\beta \gg 1$ is an adiabatic disc.

Note that the energy source terms have been chosen to be absent at $t = 0$, allowing the disc to be initialized close to steady state. The $\mathcal{C}$ function attempts to restore the initial energy density (and therefore temperature) profile. In practice, this is a cooling term at the gap edge because disc–planet interaction leads to heating.

2.2 Disc model and initial condition

The disc occupies $r \in [r_{in}, r_{out}]$ and $\phi \in [0, 2\pi]$. The initial disc is axisymmetric with surface density profile

$$\Sigma(r) = \Sigma_{ref} \left(\frac{r}{r_{in}} \right)^{-s} \left[1 - \sqrt{\frac{r_{in}}{r + H_i(r_{in})}} \right], \tag{6}$$

where the power-law index $s = 2$, $H(r) = c_{iso} \Omega_k$ defines the disc scaleheight where $c_{iso} = \sqrt{p/\Sigma}$ is the isothermal sound-speed. The disc aspect ratio is defined as $h \equiv H/r$ and initially $h = 0.05$. For a non-self-gravitating disc, the surface density scale Σ_{ref} is arbitrary.

The initial azimuthal velocity $v_{\phi i}$ is set by centrifugal balance with pressure forces and stellar gravity. For a thin disc, $v_\phi \simeq r\Omega_k$. The initial radial velocity is $v_r = 3\nu/r$, where $\nu = \hat{\nu} r_{in}^2 \Omega_k(r_{in})$, and we adopt $\hat{\nu} = 10^{-9}$, so that $|v_r/v_\phi| \ll 1$ and the initial flow is effectively only in the azimuthal direction. With this value of physical viscosity, the only source of heating is through compression, shock heating (via artificial viscosity) and the $\mathcal{C}$ function when $e/\Sigma < e_i/\Sigma_i$.

2.3 Planet potential

The planet potential is given by

$$\Phi_p = -\frac{GM_p}{\sqrt{|\boldsymbol{r} - \boldsymbol{r}_p|^2 + \epsilon_p^2}}, \tag{7}$$

where M_p is the planet mass, and we fix $q \equiv M_p/M_* = 10^{-3}$ throughout this work. This corresponds to a Jupiter-mass planet if $M_* = M_\odot$. The planet's position in the disc $\boldsymbol{r}_p = (r_p, \phi_p)$ and $\epsilon_p = 0.5 r_h$ is a softening length with $r_h = (q/3)^{1/3} r_p$ being the Hill radius. The planet is held on a fixed circular orbit with $r_p = 10 r_{in}$ and $\phi_p = \Omega_k(r_p) t$. This also defines the time unit $P_0 \equiv 2\pi/\Omega_k(r_p)$ used to describe results.

3 NUMERICAL EXPERIMENTS

The disc–planet system is evolved using the FARGO-ADSG code (Baruteau & Masset 2008a,b). This is a modified version of the

original FARGO code (Masset 2000) to include the energy equation. The code employs a finite-difference scheme similar to the FZEUS code (Stone & Norman 1992), but with a modified azimuthal transport algorithm to circumvent the time-step restriction set by the fast rotation speed at the inner disc boundary. The disc is divided into (N_r, N_ϕ) zones in the radial and azimuthal directions, respectively. The grid spacing is logarithmic in radius and uniform in azimuth.

3.1 Cooling prescription

In this work we only vary one control parameter: the cooling time. The cooling parameter β is chosen indirectly through the parameter $\tilde{\beta}$ such that

$$t_c(r_p + x_s) = \beta \Omega_k^{-1}(r_p + x_s) = \tilde{\beta} t_{lib}(r_p + x_s), \tag{8}$$

where x_s is the distance from the planet to its gap edge and t_{lib} is the time interval between successive encounters of a fluid element at the gap edge and the planet's azimuth. That is, we measure the cooling time in units of the time interval between encounters of a fluid element at the gap edge and the planet-induced shock.

Assuming Keplerian orbital frequencies and $x_s \ll r_p$ gives $t_{lib} \simeq 4\pi r_p/(3\Omega_{kp} x_s)$, where $\Omega_{kp} = \Omega_k(r_p)$. Therefore,

$$\beta = \tilde{\beta} \frac{4\pi r_p}{3x_s} \left(1 - \frac{3x_s}{2r_p}\right), \tag{9}$$

where $x_s \ll r_p$ was used again. We use $x_s = 2r_h$ in equation (9). For a planet mass with $q = 10^{-3}$, equation (9) then gives $\beta \simeq 23.9\tilde{\beta}$. In terms of planetary orbital periods, this is

$$t_c(r) = \frac{\beta}{2\pi} \left(\frac{r}{r_p}\right)^{3/2} P_0 \simeq 3.8\tilde{\beta} \left(\frac{r}{r_p}\right)^{3/2} P_0. \tag{10}$$

3.2 Diagnostic measures

3.2.1 *Generalized PV*

The generalized PV is defined as

$$\tilde{\eta} = \frac{\kappa^2}{2\Omega\Sigma} \times S^{-2/\gamma}, \tag{11}$$

where $\kappa^2 = r^{-3}\partial_r(r^4\Omega^2)$ is the square of the epicyclic frequency, $\Omega = v_\phi/r$ is the angular speed and $S \equiv p/\Sigma^\gamma$ is the entropy. The first factor is the usual PV (or vortensity).

The generalized PV appears in the description of the linear stability of radially structured adiabatic discs (Lovelace et al. 1999; Li et al. 2000), where the authors show an extremum in $\tilde{\eta}$ may lead to a dynamical instability, the RWI. In a barotropic disc where $p = p(\Sigma)$, the entropy factor is absent and the important quantity is the PV.

3.2.2 *Fourier modes*

The RWI is characterized by exponentially growing perturbations. Though in this paper we do not consider a formal linear instability calculation, modal analysis will be useful to analyse the growth of perturbations with different azimuthal wavenumbers, which is associated with the number of vortices initially formed by the RWI.

The Fourier transform of the time-dependent surface density is

$$\Sigma_m(r, t) = \int_0^{2\pi} \Sigma(r, \phi, t)\, e^{-im\phi}\, d\phi \tag{12}$$

where m is the azimuthal wavenumber. We define the growth rate σ of the mth component of the surface density through

$$\frac{d\langle|\Sigma_m|\rangle_r}{dt} = \sigma \langle|\Sigma_m|\rangle_r, \tag{13}$$

where $\langle|\cdot|\rangle_r$ denotes the average of the absolute value over a radial region of interest. By using equation (13) the growth rates of the unstable modes can be found from successive spatial Fourier transforms over an appropriate period of time.

3.2.3 *Rossby number*

The Rossby number,

$$\mathrm{Ro} = \frac{\hat{z} \cdot \nabla \times \boldsymbol{v} - \langle \hat{z} \cdot \nabla \times \boldsymbol{v} \rangle_\phi}{2\langle\Omega\rangle_\phi}, \tag{14}$$

is a dimensionless measure of relative vorticity. Here $\langle \cdot \rangle_\phi$ denotes an azimuthal average. Values of $\mathrm{Ro} < 0$ correspond to anticyclonic rotation with respect to the background shear and thus can be used to identify vortices and quantify its intensity.

4 GROWTH OF NON-AXISYMMETRIC MODES WITHOUT THE INFLUENCE OF THE PLANET

In this section, the planet is introduced at $t = 20P_0$ and its potential is switched on over $10P_0$. At $t = 30P_0$ we switch off the planet potential and azimuthally average the surface density, energy and velocity fields. (At this point the planet has carved a partial gap and the RWI has not yet occurred.) Effectively, we initialize the disc with a gap profile. We then perturb the surface density in the outer disc ($r > r_p$) and continue to evolve the disc. We impose sinusoidal perturbations with azimuthal wavenumbers $m \in [1, 10]$ and random amplitudes within ± 0.01 times the local surface density. This procedure allows us to analyse the growth of non-axisymmetric modes associated with the gap, but without complications from non-axisymmetry arising directly from disc–planet interaction (i.e. planet-induced wakes).

Note that these 'planet-off' simulations are not linear stability calculations because the cooling term in our energy equation restores the initial temperature profile corresponding to constant $H/r = 0.05$, rather than the heated gap edge. However, we will examine a nearly adiabatic simulation in Section 4.3.1, which is closer to a proper linear problem.

Simulations here employ a resolution of $(N_r, N_\phi) = (1024, 2048)$ with open boundaries at $r = r_{in}$ and $r_{out} = 25r_{in}$. We compare cases with $\tilde{\beta} = 0.1, 1, 10$ corresponding to fast, moderately, and slowly cooled discs.

4.1 Gap structure

We first compare the gap structures formed by planet–disc interaction as a function of the cooling time. The azimuthally averaged gap profiles are shown in Fig. 1 for different values of $\tilde{\beta}$. Gaps formed with lower $\tilde{\beta}$ (faster cooling) are deeper with steeper gradients at the gap edges. Faster cooling rates also increase (decrease) the surface density maxima (minima). However, a clean gap does not form in this short time period.

Increasing $\tilde{\beta}$ leads to higher disc aspect ratios $h = H/r$, i.e. higher temperatures. Heating mostly occurs at the gap edges due to planet-induced spiral shocks. Increasing the cooling time-scale implies that this heat is retained in the disc. In the inviscid limit, the gap-opening condition is $r_h \gtrsim H$ or $q \gtrsim 3h^3$ (Crida et al. 2006), which indicates

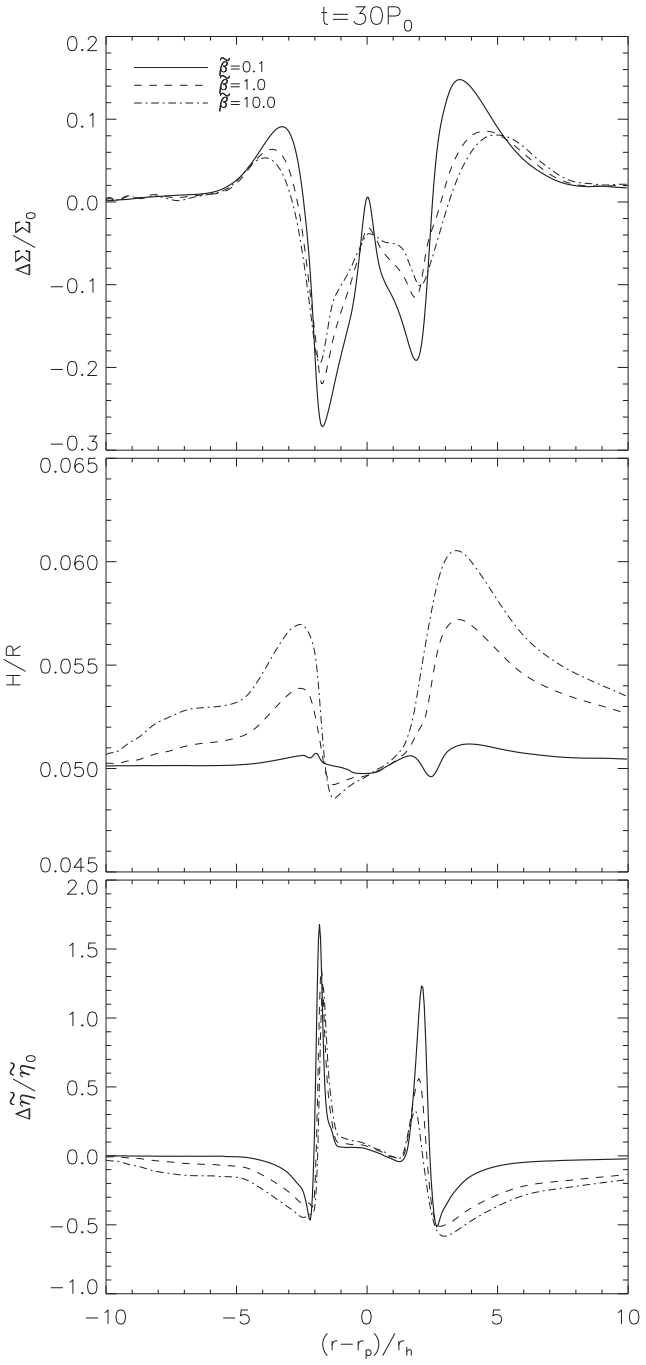

Figure 1. Azimuthally averaged gap profiles at $t = 30P_0$ for the initial partial gap opened before instability emerges for fast (solid, $\tilde{\beta} = 0.1$), moderate (dashed, $\tilde{\beta} = 1$), and slow cooling (dashed-dot, $\tilde{\beta} = 10$). The relative surface density perturbation (top), disc aspect ratio (middle) and generalized vortensity perturbation (bottom) are shown.

that for hotter discs (higher h), it becomes more difficult for a planet of fixed q to open a gap. This explains the shallower gaps in surface density when $\tilde{\beta}$ is increased.

The important consequence of a heated gap edge is that the generalized vortensity profiles, $\tilde{\eta}$, becomes smoother with increasing cooling times, with the extrema becoming less pronounced. Previous locally isothermal disc–planet simulations show the RWI associated with PV minima (Li et al. 2005; Lin & Papaloizou 2010). We can therefore expect the RWI to be associated with minima in the generalized vortensity (corresponding to local surface density maxima) in the non-isothermal case. Because the extrema are less sharp, the RWI is expected to be weaker and the gap to be more stable with longer cooling times.

However, we remark that the change in the gap structure becomes less significant at long cooling times, as Fig. 1 shows that the profiles with $\tilde{\beta} = 1$ and $\tilde{\beta} = 10$ are similar. This implies that the effect of cooling time-scale on the RWI through the set-up of the gap profile, becomes less important for large $\tilde{\beta}$.

4.2 Axisymmetric stability

The initial planet–disc interaction form bumps and grooves in the gap profiles which can potentially be unstable due to axisymmetric instabilities. The generalized local axisymmetric stability condition is the Solberg–Hoiland criterion,

$$\kappa^2 + N^2 \geq 0 \tag{15}$$

where

$$N^2 = \frac{1}{\Sigma}\frac{\partial P}{\partial r}\left(\frac{1}{\Sigma}\frac{\partial \Sigma}{\partial r} - \frac{1}{\gamma P}\frac{\partial P}{\partial r}\right) \tag{16}$$

is the square of the Brunt–Väisälä frequency. At the outer gap edge $r = r_\mathrm{p} + 2.5r_\mathrm{h}$, where the RWI is excited (see below), we find $\kappa^2 + N^2$ reaches local minimum with a value $\sim 0.45\,\Omega^2(r_\mathrm{p})$ for all $\tilde{\beta}$. The Brunt–Väisälä frequency at the outer gap edge is $N \sim 0.1\,\Omega(r_\mathrm{p})$, decreasing marginally with longer cooling rate. The Solberg–Hoiland criterion is similarly satisfied for the entire 2D disc throughout the simulations. Thus for all values of $\tilde{\beta}$ the planet-induced gaps are stable to axisymmertic perturbations.

4.3 Non-axisymmetric instability

We now examine the evolution of the gap for $t > 30P_0$, with the planet potential switched off, but with an added surface density perturbation. For all three cooling times $\tilde{\beta} = 0.1,\ 1.0,\ 10$, we observe exponential growth of non-axisymmetric structures. An example is shown in Fig. 2 for $\tilde{\beta} = 10$. We characterize these modes with an

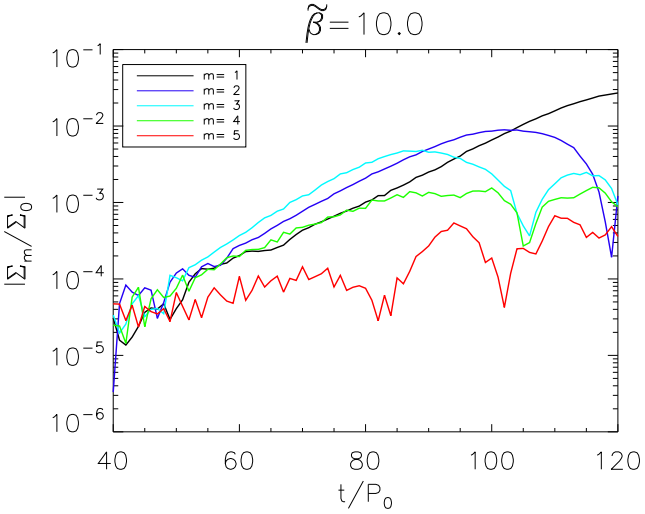

Figure 2. Evolution of azimuthal Fourier modes of disc surface density, non- dimensionalized by the initial axisymmetric component $\Sigma_0(t = 0)$, for the 'planet-off' simulation with $\tilde{\beta} = 10$. Colours correspond to different m values. The $m = 3$ component is the fastest growing mode during linear growth with a growth rate of $\gamma = 0.017\Omega(r_\mathrm{p})$.

Table 1. Dominant mode and growth rates for $\tilde{\beta} = 0.1, 1.0, 10.0$ (fast, moderate and slow cooling) values during 'planet-off' simulations.

$\tilde{\beta} = 0.1$		$\tilde{\beta} = 1.0$		$\tilde{\beta} = 10.0$	
m	$10^2\sigma/\Omega(r_p)$	m	$10^2\sigma/\Omega(r_p)$	m	$10^2\sigma/\Omega(r_p)$
6	7.3	3	2.0	1	1.1
7	7.8	4	2.2	2	1.6
8	7.9	5	2.3	3	1.7
9	7.9	6	1.6	4	1.2
10	6.8	7	1.1	5	0.1

azimuthal wavenumber m and growth rate $\sigma(m)$ as defined by equations (12) and (13). Mode amplitudes were averaged over $r - r_p \in [2, 5]r_h$. Table 1 lists the growth rates measured during linear growth for five values of m centred around that with maximum growth rate.

Table 1 show that as $\tilde{\beta}$ is increased from 0.1 to 10 the dominant azimuthal Fourier mode decreases from $m = 9$ to 3 and the respective growth rate decreases from $\gamma/\Omega(r_p) = 0.079$ to 0.017. However, despite two orders of magnitude increase in the cooling time, the instability remains dynamical with characteristic growth time $\lesssim 10P_0$. Snapshots of the instability in for the different $\tilde{\beta}$ are shown in Fig. 3.

These 'planet-off' simulations show that gap edges become more stable with longer cooling times. This is expected because larger $\tilde{\beta}$ results in hotter gap profiles at $t = 30P_0$ with less pronounced generalized vortensity minima. Stabilization with increased cooling time is therefore due to a smoother basic state for the instability, as it is more difficult for the planet to open a gap if the disc is allowed to heat up.

For completeness we also simulated a locally isothermal disc with $h = 0.05$ where the sound speed is kept strictly equal to its initial value. This simulation yield a most unstable growth rate $\sigma/\Omega(r_p) \simeq 0.05$ at $m = 5$, compared with a value of 0.085 at $m = 6$ for a corresponding simulation that includes the energy equation but with rapid cooling $\tilde{\beta} = 0.01$. However, the vortex evolution is similar.

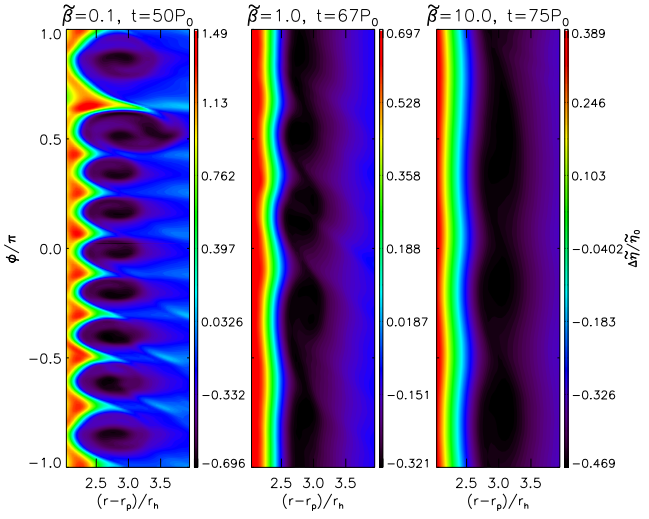

Figure 3. Generalized vortensity perturbation (relative to $t = 0$) for cases of $\tilde{\beta} = 0.1$, 1, 10 (left, middle, right) during the growth of non-axisymmetric modes. The planet potential has been switched off. The number of vortices decrease as $\tilde{\beta}$ increases. Note that snapshots are taken later for increasing $\tilde{\beta}$ because it takes longer for the vortices to grow and become visible with increasing cooling time.

4.3.1 *Nearly adiabatic discs*

The above-mentioned 'planet-off' simulations are not formally linear stability calculations, because the cooling time is comparable or shorter than the instability growth time, $t_c \lesssim \gamma^{-1}$. Thus the disc cools back to its initial temperature corresponding to $h = 0.05$ before or during the instability growth, so we do not have a steady basic state to formulate a standard linear stability problem.

In order to capture the effect of a heated gap edge, we ran a simulation with $\tilde{\beta} = 100$, corresponding to an almost adiabatic disc. In this simulation the cooling rate is slow enough that the gap temperature profile (e.g. middle panel of Fig. 1) changes only marginally over the instability growth time-scale.

We find very similar gap profiles and mode growth rates for $\tilde{\beta} = 100$ as with $\tilde{\beta} = 10$. At $t = 30P_0$, the disc only heats up to values $h \simeq 0.06$ in the nearly adiabatic case. This is close to the original temperature of $h = 0.05$, so linear growth rates are not expected to change significantly (Li et al. 2000).

According to Li et al. (2000), increasing h increases linear growth rates of the RWI because it is pressure driven. However, in the case of disc–planet interaction, increasing h has a stabilizing effect through the setting up the gap profile because it results in smoother gap edges. The fact that we observe smaller growth rates as h is increased indicates that for planetary gaps, the importance of h on the *linear* RWI is through setting up the gap profile, i.e. basic state for the instability (as opposed to the linear response).

4.4 Long-term evolution

We also extended these 'planet-off' simulations into the non-linear regime. After the linear growth phase of the vortices, vortex merging takes hold on time-scales of up to $150P_0$, until there is one vortex left. We find the vortex merging time is dependent on the growth rates of the modes and saturation time-scales, with the slowest growing modes in $\tilde{\beta} = 10$ taking the longest to merge.

Fig. 4 shows evolution of the $m = 1$ surface density component, which represents the amplitude of the post-merger single vortex. For completeness we also ran intermediate cases with $\tilde{\beta} = 0.5$ and 5.0. The amplitude of the initially formed vortex was found to decrease with increased cooling rate. The vortices simply decay on a

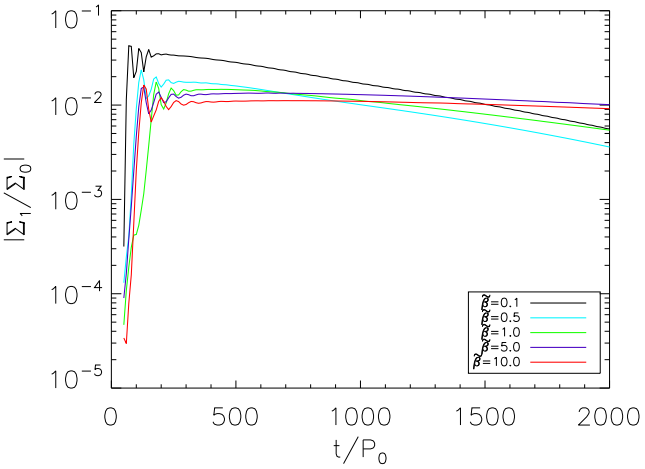

Figure 4. Long-term simulations without the planet potential after the gap is set up. The $m = 1$ surface density component, non-dimensionalized by the initial $m = 0$ component, at the outer gap edge is shown as a function of the cooling time-scale.

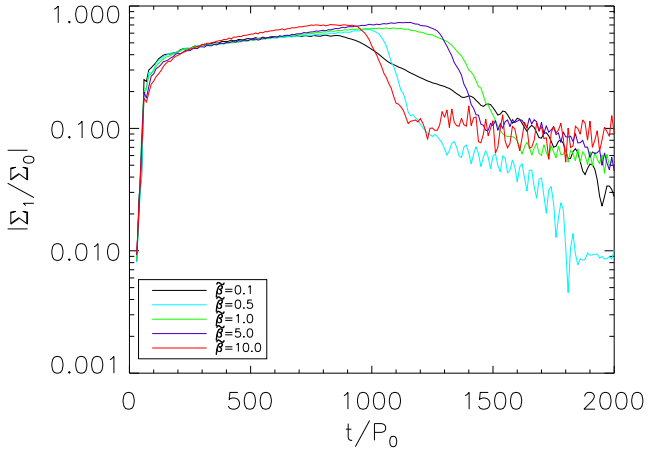

Figure 5. Evolution of the non-dimesnionalized $m = 1$ surface density component for long-term simulations with the planet potential kept on. Note there is vortex growth after the initial linear growth, which contrasts to Fig. 4, where vortices decay in the absence of continuous disc–planet interaction.

time-scale of $O(10^3)$ orbits with faster decay for stronger vortices (which are obtained with faster cooling rates).

This decay is probably due to numerical viscosity. During the slow decay the vortex elongates (weakens) while its radial width remains $O(H)$, so its surface density decreases. In addition, for $\tilde{\beta} = 0.1,\ 0.5$ and 1.0 we also observe the appearance of spiral waves associated with the vortex, which may contribute to its dissipation (see below). We will see in the next section that this decay after linear growth is very different to when the planet potential is kept on.

5 NON-LINEAR EVOLUTION OF GAP-EDGE VORTICES WITH FINITE COOLING TIME

We now examine long-term simulations of gap-edge vortices for $\tilde{\beta} = 0.1, 0.5, 1, 5, 10$. (Additional cases are presented in Section 5.4 when examining vortex lifetimes as a function of $\tilde{\beta}$.) The planet potential is kept on throughout. We employ a grid with $(N_r, N_\phi) = (512, 1024)$ in order for these simulations to be computationally feasible. We also use a larger disc with $r_{\rm out} = 45r_{\rm in}$ to minimize boundary effects on vortex evolution, and apply open boundaries at $r = r_{\rm in}, r_{\rm out}$.

We comment that lower resolution simulations with $(N_r, N_\phi) = (256, 512)$ show similar behaviour and trends as the high-resolution runs reported below.

5.1 Generic evolution

The linear growth of the RWI and vortex formation is followed by vortex merging. We now find merging time-scales independent of $\tilde{\beta}$, and by $60P_{\rm o}$ only one vortex remains. The evolution of the amplitude of the $m = 1$ surface density component, averaged over $r - r_{\rm p} \in [2, 10]r_{\rm h}$, is shown in Fig. 5 for different $\tilde{\beta}$. The initial, post-merger vortex amplitude is found to be weaker for longer cooling rates (which have smaller linear growth rates).

In all cases the system remains in a quasi-steady state for $\gtrsim 800P_0$ with a single vortex circulating the outer gap edge at the local Keplerian frequency. Fig. 6 shows a typical plot of the relative surface density perturbation in this state. During this stage, the vortex intensifies. This is better shown in Fig. 7 as the evolution of Rossby numbers measured at the vortex centres. The Rossby

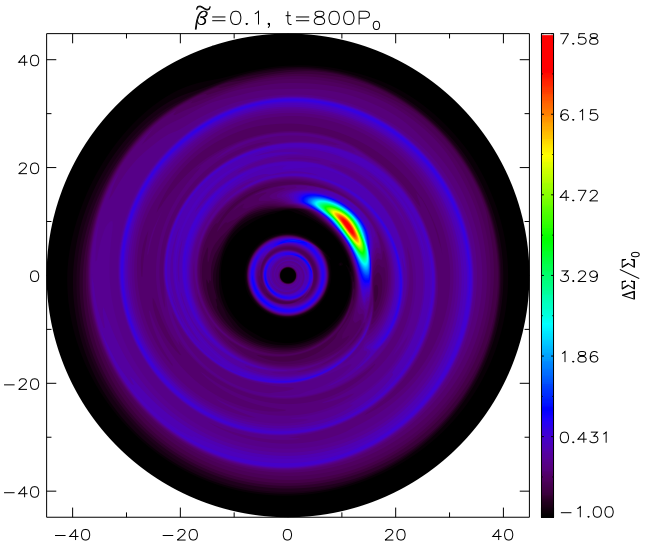

Figure 6. Relative surface density perturbation for the $\tilde{\beta} = 0.1$ case during quasi-steady state with a single vortex at the outer gap edge. The plot for other values of the cooling time $\tilde{\beta}$ are similar. The decrease in the surface density near $r \sim 40r_{\rm in}$ arises from mass-loss due to the open boundary condition imposed at $r_{\rm out}$.

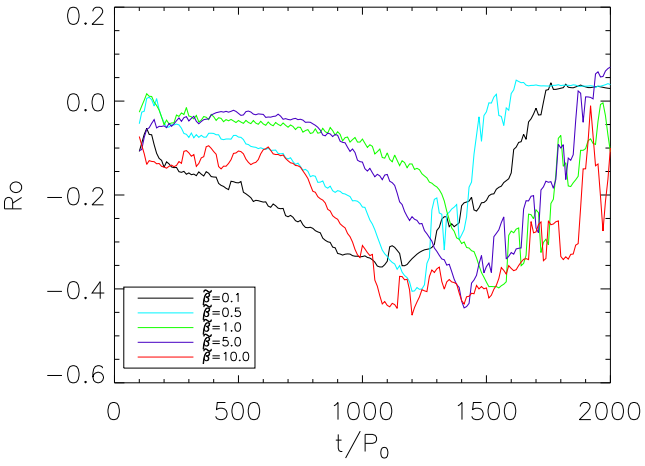

Figure 7. Evolution of Rossby numbers at the centres of the vortices formed in discs with different cooling rates. A negative Rossby number implies anticyclonic motion. Boxcar averaging was used to remove contributions from the planet-induced spiral shock.

number increases in magnitude during quasi-steady state, but the maximum |Ro| is similar for all $\tilde{\beta}$: the vortex reaches a characteristic value of Ro ≈ -0.35 for $\tilde{\beta} = 0.1$ and Ro ≈ -0.45 for $\tilde{\beta} = 10$.

We find the vortices become significantly overdense. Fig. 8 plots the surface density perturbation measured at the vortex centres, showing $\Delta\Sigma/\Sigma_0 \gtrsim 7$ for all cases of $\tilde{\beta}$ in quasi-steady state, and $\max(\Delta\Sigma/\Sigma_0) \sim 11$ for $\tilde{\beta} = 5$. The maximum overdensity typically increases with longer cooling times, despite the vortices are initially weaker at formation with increasing $\tilde{\beta}$. The large increase in the surface density is due to vortex growth as there is continuous generation of vorticity by planet–disc interaction. This is supported by the observation that in the previous simulations without the planet, the amplitude of the post-merger vortex does not grow (Fig. 4).

Fig. 5 shows that the duration of the quasi-steady state varies with the cooling rate: for $\tilde{\beta} = 0.1$ and 10, the vortex amplitude begins to decay around $t \sim 800P_0$, while for $\tilde{\beta} = 1,\ 5$ the decay begins

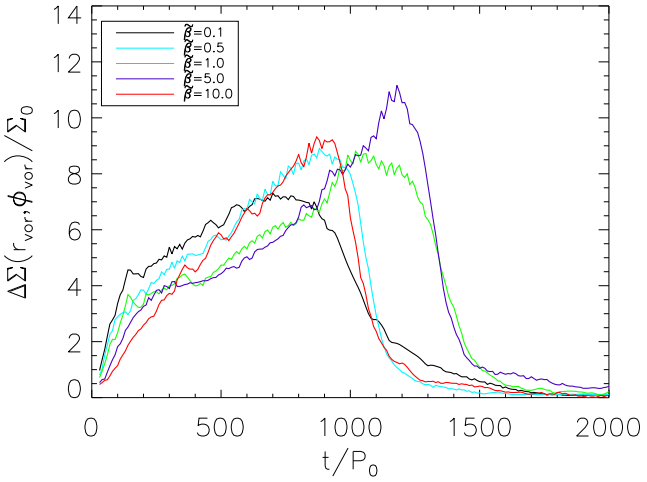

Figure 8. Average value of the relative surface density perturbation at vortex centres for various cooling times. Initial vortex overdensities decrease with cooling rate while vortex growth rates increase with cooling rate.

at $t \sim 1200P_0$. This non-monotonic dependence suggests that there exists an optimal cooling rate to maximize the vortex lifetime. We will discuss this issue further in Section 5.4. Note the decay time-scale can be long with rapid cooling: for $\tilde{\beta} = 0.1$ it takes $\sim 400P_0$ whereas for $\tilde{\beta} = 10$ it takes $\sim 100P_0$ for the $m = 1$ amplitude to decay significantly after reaching maximum.

5.2 Additional analysis on vortex decay

In this subsection, we examine the vortex decay observed in our simulations in more detail. Fig. 9 show snapshots of the vortex for the case $\tilde{\beta} = 1$. The plots show the surface density perturbation and the surface density gradient during quasi-steady state ($t = 700P_0$), when the $m = 1$ amplitude begins to decrease ($t = 1300P_0$) and just after the rapid amplitude decay ($t = 1510P_0$).

In quasi-steady ($t = 700P_0$) the vortex is elongated with a vortex aspect ratio ≈4, but becomes more compact approaching a ratio of 2 during its decay ($t = 1310P_0$). Note in Fig. 9 the appearance of

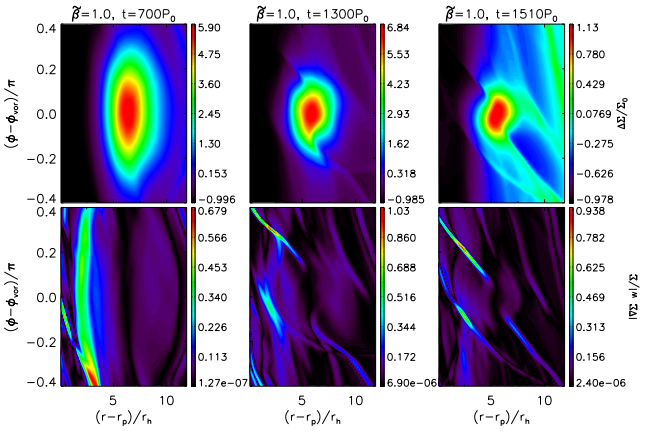

Figure 9. The vortex in the case with $\tilde{\beta} = 1$ during quasi-steady state (left), start of decay (middle) and just after the decay in the $m = 1$ amplitude (right). The surface density perturbation (top) and the associated surface density gradient (bottom) are shown. Wake-like features corresponding to large density gradients are found to originate from the vortices during the late phase of their quasi-steady states and into dissipation times. This plot is to be considered in conjunction with Fig. 5.

wakes extending from either side of the vortex at $t = 1300P_0$. These wakes correlate with large gradients in surface density (bottom panel), and are first seen in the latter half of the quasi-steady state. We find the time at which the vortex begins to decay coincides with the emergence of these wakes.

During the quasi-steady state the vortex orbits at $r \sim r_p + 6r_h$. We do not see significant vortex migration at this stage, since the vortex is located at a surface density maximum (Paardekooper, Lesur & Papaloizou 2010). However, simultaneous with the appearance of the wakes, we observe the vortex begins to migrate inwards to $r \sim r_p + 5r_h$.

During quasi-steady state the average value of the surface density gradient along the wakes is $|w_s \nabla\Sigma/\Sigma| \sim 0.4$, where $w_s \simeq 0.1$ (code units) is a typical length-scale of the surface density variation across the wake. Just before the $m = 1$ amplitude begins to decrease, we observe that this quantity sharply increases to ∼0.6, and remains around this value until the vortex dies out, at which point the associated Rossby number begins decreasing to zero. After the vortex reaches small amplitudes ($1 \lesssim \Delta\Sigma/\Sigma$), it migrates out to $r \sim r_p + 6.5r_h$.

We also measured large increases in the Mach number near the vortex as the $m = 1$ surface density amplitude reaches maximum and begins to decay. Fig. 10 plots the Mach number $M = |\boldsymbol{v} - \boldsymbol{v}_{vor}|/c_s$, where $\boldsymbol{v}_{vor}$ corresponds to the bulk velocity of the vortex around the disc. Values in Fig. 10 have been averaged over a region within $2H$ of the vortex centre. During the quasi-steady state the Mach number increases steadily, and for all cases M maximizes about $\sim 100P_0$ after the $m = 1$ surface density amplitude starts to decay.

Putting the above-mentioned observations together, we suggest that vortex decay (in the $m = 1$ surface density amplitude) is due to shock formation by the vortex. When the vortex reaches large amplitude, it begins to induce shocks in the surrounding fluid, as supported by the increase in Mach number and the appearance of wakes with large surface density gradients. The vortex may lose energy through shock dissipation. In addition, a strong vortex (or shock formation) can smooth out the gap structure that originally gave rise to the RWI, which would oppose vortex growth. We examine this below.

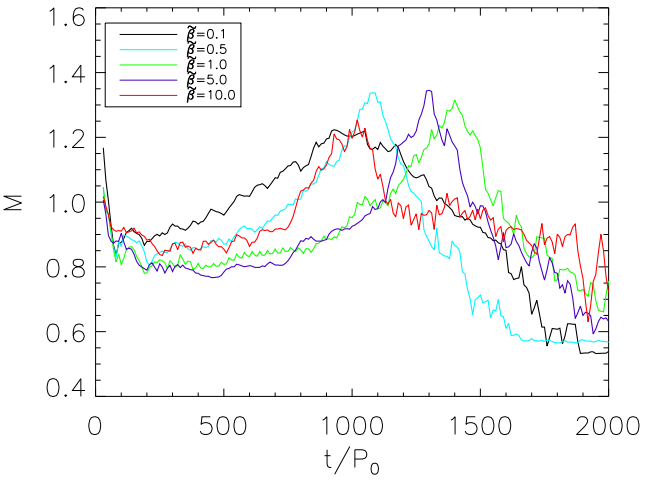

Figure 10. Mach number relative to the vortex, averaged over a region within $2H$ of the vortex centre with respect to time. This plot can be compared to the evolution of the vortex amplitude shown in Fig. 5.

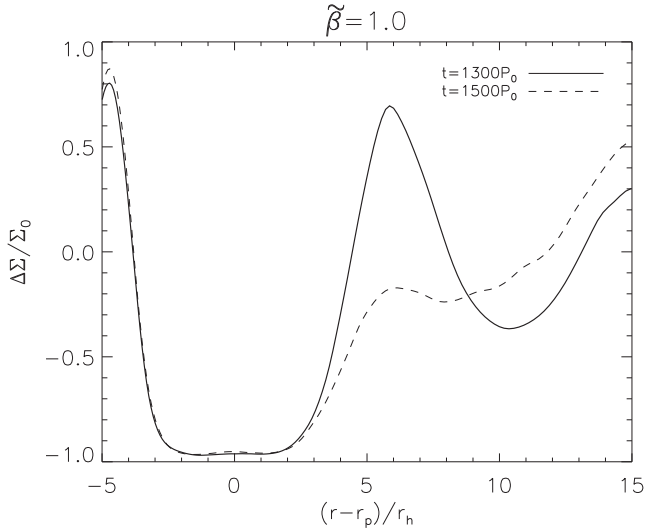

Figure 11. Azimuthally averaged profiles of the relative surface density perturbations for $\tilde{\beta} = 1.0$ before (solid) and after vortex decay (dashed). Alongside drastic reduction in the outer gap maxima, vortex decay smooth out the sharp outer gap edge.

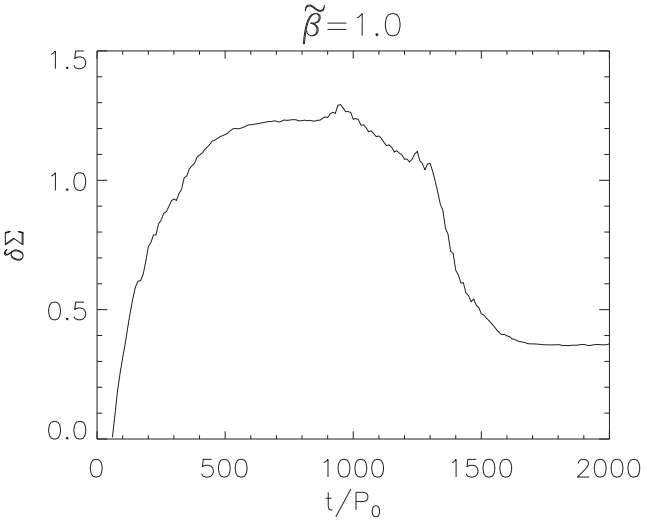

Figure 12. Non-dimensional measure of the surface density gradient at the outer gap edge $\tilde{\beta} = 1.0$. During the vortex quasi-steady state the gap edge is found to have a large gradient and sharp peak while vortex dissipation, which occurs at $t \approx 10^3 P_0$ as seen in Fig. 5, works to smooth out the gap edge.

5.3 Vortex decay and gap structure

We find vortex decay modifies the gap structure. Fig. 11 shows the gap profile before and after vortex decay for the case $\tilde{\beta} = 1$. The vortex resides around the local surface density maximum at the outer gap edge ($r \sim r_p + 6r_h$). We see that after its amplitude has decayed ($t \sim 1500P_0$, Fig. 5), this local surface density maximum is also smoothed out.

We characterize the smoothness of the outer gap edge with a dimensionless gap edge gradient parameter

$$\delta\Sigma(t) = \left\langle \frac{\partial\langle\Sigma(t,r)\rangle_\phi}{\partial r} \cdot \frac{r}{\langle\Sigma(t=0,r)\rangle_\phi} \right\rangle_{\Delta r}, \qquad (17)$$

where $\Delta r = r \in [r_p, r_p + 6r_h]$ is the radial range of averaging, spanning from centre of the gap to the radius of the surface density maximum. A larger $\delta\Sigma$ characterizes a sharper gap edge and larger local surface density maxima.

A plot of the gradient parameter over time for the $\tilde{\beta} = 1.0$ case is shown in Fig. 12. During vortex decay, the outer gap edge is drastically smoothed out, changing from a value of $\delta\Sigma = 1.2$ during quasi-steady state to 0.4 after dissipation.

This can be interpreted as the vortex providing a viscosity; and we measure a typical alpha viscosity $\alpha = O(10^{-2})$ associated with the vortex. This acts against gap opening by the planet, and smooths out the outer surface density bump, so the condition for the RWI becomes less favourable. In order to re-launch the RWI, the surface density bump should reform. However, this is difficult as there is no more material in the planet's vicinity to clear out (Fig. 11) to form a surface density bump outside the gap. This may explain why vortices do not reform again (at least within the simulation time-scale). After full decay the aspect ratio at the outer gap edge is $h \sim 0.05$.

5.4 Vortex lifetimes as a function of cooling rate

We now examine vortex lifetimes as function of the imposed cooling times. For this study, additional simulations with $\tilde{\beta} =$ 0.01, 0.25, 0.75, 2.5, 7.5 were also performed. We define the vortex lifetime, t_{life}, as the time at which the overdensity of the vortex returns to $\Delta\Sigma/\Sigma_0 \sim 1$ *after* reaching maximum (which is of the order of the initial overdensity associated with the gap formation).

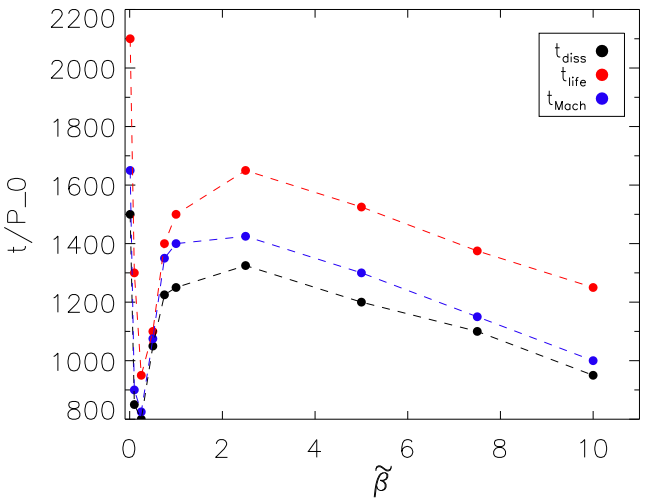

Figure 13. Characteristic time-scales associated with vortex evolution, as a function of the cooling parameter $\tilde{\beta}$: time in which the $m = 1$ surface density amplitude begins to decay, t_{diss} (black); time at which the overdensity at the vortex centre decreases to $\Delta\Sigma/\Sigma \sim 1$ after reaching maximum, t_{life} (red); and t_{Mach} is the time taken for the average Mach number around the vortex to maximize (blue).

We plot t_{life} with respect to cooling times in Fig. 13. We also plot t_{diss}: the time elapsed before the vortex to begins to dissipate (when the $m = 1$ surface density amplitude begins to decay); and t_{Mach}: the time taken for the average Mach number around the vortex to maximize.

For fast cooling rates ($\tilde{\beta} \lesssim 1$), the vortex lifetime is maximized for $\tilde{\beta} \to 0$: we find $t_{life} \approx 2100P_0$ for $\tilde{\beta} = 0.01$ and decreases

to $t_{\rm life} \approx 950P_0$ for $\tilde{\beta} = 0.25$. Note that for very small $\tilde{\beta}$, there is significant contribution to the overall vortex lifetime due to a long decay time-scale. For longer cooling times ($\tilde{\beta} \gtrsim 1$) the vortex lifetimes maximizes at $\tilde{\beta} = 2.5$ with $t_{\rm life} \approx 1650P_0$.

We comment here that a locally isothermal simulation, where the disc sound-speed is kept constant in time, was also performed for comparison. In this case we did not observe significant vortex decay within the simulation time-scale (implying $t_{\rm diss} \gtrsim 2000P_0$). We expect the corresponding vortex lifetime to exceed that for $\tilde{\beta} = 0.01$. Including an energy equation with rapid cooling (or setting γ close to unity) could still lead to discrepancies with a locally isothermal disc. This is due to the advection-creation of specific entropy within the planet's horseshoe region with the former case, thereby affecting the generalized vortensity and therefore the instability (Section 4.3) and subsequent vortex evolution. Nevertheless, a longer vortex lifetime in a locally isothermal disc would be consistent with the above-mentioned trend of increasing vortex lifetimes as $\tilde{\beta} \to 0$.

In the previous section, we observed that vortices began to decay when it starts to induce shocks. We thus suggest that the time needed for the vortex to grow to sufficient amplitude to induce shocks in the surrounding fluid, which may be considered as the duration of the quasi-steady state or $t_{\rm diss}$, is an important contribution to the overall vortex lifetime. We discuss below some competing factors that may result in a non-monotonic dependence of $t_{\rm diss}$ on the cooling rate.

5.4.1 *Factors that lengthen vortex lifetimes*

It has been shown that the amplitude at which the RWI saturates increases with the growth rate of the linear instability (Meheut, Lovelace & Lai 2013). Our 'planet-off' simulations yield slower growth rates with increasing cooling times, which suggest weaker vortices are formed initially with increasing $\tilde{\beta}$. This is consistent with the present simulations: at the beginning of the quasi-steady state ($t \sim 100P_0$) we find the overdensity at the vortex centre is $\Delta\Sigma/\Sigma_0 = 2.5$ for $\tilde{\beta} = 0.1$ and $\Delta\Sigma/\Sigma_0 = 1.48$ for $\tilde{\beta} = 10$.

The growth of the post-merger single vortex is mediated by disc–planet interaction. However, gap opening becomes more difficult in a hotter disc, and we find the generalized vortensity profiles are smoother with increasing $\tilde{\beta}$. This opposes the RWI. Furthermore, the vortex should reach larger amplitudes to induce shocks on account of the increased sound speed.

These considerations suggest, with increased cooling times, it takes longer for the post-merger vortex grow to sufficient amplitude to induce shocks and dissipate. This factor contributes to a longer quasi-steady state with increasing $\tilde{\beta}$.

5.4.2 *Factors that shorten vortex lifetimes*

Note in Figs 5 and 8, the vortex growth during the quasi-steady state is actually faster for $\tilde{\beta} = 10$ than for $\tilde{\beta} = 5$. For example, at $t \sim 500P_0$ the vortex with $\tilde{\beta} = 10$ has a larger amplitude than for $\tilde{\beta} = 5$. This is also reflected in Fig. 10, where the Mach number reaches its maximum value sooner for $\tilde{\beta} = 10$ than for $\tilde{\beta} = 5$.

This observation is consistent with the RWI being favoured by higher temperatures (Li et al. 2000; Lin 2012) through the perturbations (as opposed to its effect through the set-up of the gap profile discussed previously), which corresponds to longer cooling times in our case. While our 'planet-off' simulations indicate this is unimportant for the linear instability, it may have contributed significantly to the vortex growth during quasi-steady state at very long cooling times (e.g. $\tilde{\beta} = 10$). This effect shortens the vortex lifetime by allowing it to grow faster and induce shocks sooner.

6 SUMMARY AND DISCUSSION

In this paper, we have carried out numerical simulations of non-isothermal disc–planet interaction. Our simulations were customized to examine the effect of a finite cooling time on the stability of gaps opened by giant planets to the so-called vortex instability or RWI. To do so, we included an energy equation with a cooling term that restores the disc temperature to its initial profile on a characteristic time-scale $t_{\rm c}$. We studied the evolution of the gap stability as a function of $t_{\rm c}$. This is a natural extension to previous studies of on gap stability, which employ locally or strictly isothermal equations of state. We considered the inviscid limit which favours the RWI (Li et al. 2009; Fu et al. 2014) and avoids complications from viscous heating other that shock heating. However, this means that the vortex lifetimes observed in our simulations are likely longer than in realistic discs with non-zero physical viscosity.

We considered two types of numerical experiments. We first used disc–planet interaction to self-consistently set up gap profiles, which were then perturbed and evolved without further the influence of the planet potential. This procedure isolates the effect of cooling on gap stability through the set-up of the initial gap profile. We find that as the cooling time $t_{\rm c}$ is increased, the gaps became more stable, with lower growth rates of non-axisymmetric modes and the dominant azimuthal wavenumber also decreases. This is consistent with the notion that increasing $t_{\rm c}$ leads to higher temperatures or equivalently the disc aspect ratio h, which opposes gap opening by the planet. This means that the gaps opened by the planet in a disc with longer $t_{\rm c}$ are smoother and therefore more stable to the RWI.

In the second set of calculations, we included the planet potential throughout the simulations and examined the long-term evolution of the gap-edge vortex that develops from the RWI. The vortex reaches a quasi-steady state lasting $O(10^3)$ orbits. Unlike the 'planet-off' simulations, in which vortices decay after linear growth and merging, we find that with the planet potential kept on, the vortex amplitude grows during this quasi-steady state, during which no vortex migration is observed, until it begins to induce shocks, after which the vortex amplitude begins to decay.

For our main simulations with dimensionless cooling times $\tilde{\beta} \geq 0.1$, the duration of the quasi-steady state increases with increasing cooling time-scales until a critical value, beyond which this quasi-steady state shortens again. We find the time-scale for the vortex to decay after reaching maximum amplitude can be long for small $\tilde{\beta}$, which contributes to a long overall vortex lifetime with rapid cooling. We do observe vortex migration during its decay, which may influence this decay time-scale.

We suggest a non-monotonic dependence of the quasi-steady state on the cooling time-scale $\tilde{\beta}$ can be attributed to the time required for the vortex to grow to sufficient amplitude to induce shocks in the surrounding fluid, thereby losing energy and also smooth out the gap edge.

For short cooling time-scales, the planet is able to open a deeper gap which favours the RWI, leading to stronger vortices. For long cooling time-scales, we find the vortex grows faster during the quasi-steady state. In accordance with previous stability calculations (Li et al. 2000), we suggest the latter is due to the RWI being favoured with increasing disc temperature, and that this effect overcomes weaker gap opening for sufficiently long cooling times. These competing factors imply for both short and long cooling time-scales, the

vortex reaches its maximum amplitude, shock and begins to decay, sooner than intermediate cooling time-scales.

(However, for very rapid cooling, e.g. $\tilde{\beta} = 0.01$, the quasi-steady state is also quite long. This suggests that the above-mentioned effects themselves do not have a simple dependence on the cooling time-scale when considering $\tilde{\beta} \to 0$ and/or that other factors become important in this limit. This should be investigated in future works.)

We remark that a non-monotonic dependence of the vortex lifetime was also reported by Fu et al. (2014), who performed locally isothermal disc–planet simulations with different values of the disc aspect ratio. In their simulations, the optimum aspect ratio is $h = 0.06$. In our simulations, h is a dynamical variable, but by analysing the region where the vortex is located ($r - r_{\rm p} \in [2, 10]r_{\rm h}$), we find for a dimensionless cooing time-scale of $\tilde{\beta} = 2.5$, which has the longest vortex lifetime in the presence of moderate cooling, that $h \approx 0.058$ on average. Our result is thus consistent with Fu et al. (2014).

6.1 Caveats and outlooks

There are several outstanding issues that needs to be addressed in future work.

Convergence. Although lower resolution simulations performed in the early stages of this project gave similar results (most importantly, the non-monotonic dependence of vortex lifetimes on the cooling time-scale), we did find the lower resolution typically yield longer vortex lifetimes than that reported in this paper. This could be due to weaker RWI with low resolution. It will be necessary to perform even higher resolution simulations in order to obtain quantitatively converged vortex lifetimes.

Orbital migration. We have held the planet fixed on a circular orbit. However, gap-edge vortices are known to exert significant, oscillatory torques on the planet (Li et al. 2009) which can lead to complex orbital migration. This will likely affect vortex lifetimes as it may alter the planet–vortex separation, as well as leading to direct vortex–planet interactions (Lin & Papaloizou 2010; Ataiee et al. 2014). Thus, future simulations should allow the planet to freely migrate. Similarly, the role of vortex migration on its lifetime should be clarified.

Cooling model. Our prescription for the disc heating/cooling is convenient to probe the full range of thermodynamic response of the disc. However, in order to calculate vortex lifetimes in actual protoplanetary discs, an improved thermodynamics treatment, e.g. radiative cooling based on realistic disc temperature, density, opacity models, etc., should be used in future work.

Self-gravity. We have ignored disc self-gravity in this study. Based on linear calculations, Lovelace & Hohlfeld (2013) concluded self-gravity to be important for the RWI when the Toomre parameter $Q < O(1/h)$, or $Q \lesssim 20$ for $h \sim 0.05$, as was typically considered in this work. This suggests that self-gravity may affect vortex lifetimes even when Q is not small. In particular, given that we observe vortices can reach significant overdensities (up to almost an order of magnitude), it will be important to include disc self-gravity in the future.

Three-dimensional (3D) effects. A vortex in a 3D disc may be subject to secondary instabilities that destroy them (Lesur & Papaloizou 2009; Railton & Papaloizou 2014). This may be an important factor in determining gap-edge vortex lifetimes in realistic discs. For example, if these secondary instabilities sets in before the vortex grows to sufficient amplitude to shock, then the dependence of the vortex lifetime on the cooling time-scale will be its effect through the 3D instability (as opposed to the effect on the RWI itself, which is a 2D instability). This problem needs to be clarified with full 3D disc–planet simulations.

ACKNOWLEDGEMENTS

This project was initiated at the Canadian Institute for Theoretical Astrophysics (CITA) 2014 summer student programme. The authors thank the anonymous referee for an insightful report. Computations were performed on the GPC supercomputer at the SciNet HPC Consortium. SciNet is funded by the Canada Foundation for Innovation under the auspices of Compute Canada; the Government of Ontario; Ontario Research Fund - Research Excellence; and the University of Toronto.

REFERENCES

Ataiee S., Dullemond C. P., Kley W., Regály Z., Meheut H., 2014, A&A, 572, A61
Barge P., Sommeria J., 1995, A&A, 295, L1
Baruteau C., Masset F., 2008a, ApJ, 672, 1054
Baruteau C., Masset F., 2008b, ApJ, 678, 483
Baruteau C., Masset F., 2013, in Souchay J., Mathis S., Tokieda T., eds, Lecture Notes in Physics, Vol. 861, Tides in Astronomy and Astrophysics. Springer-Verlag, Berlin, p. 201
Bryden G., Chen X., Lin D. N. C., Nelson R. P., Papaloizou J. C. B., 1999, ApJ, 514, 344
Casassus S. et al., 2013, Nature, 493, 191
Crida A., Morbidelli A., Masset F., 2006, Icarus, 181, 587
de Val-Borro M., Artymowicz P., D'Angelo G., Peplinski A., 2007, A&A, 471, 1043
Debes J. H., Jang-Condell H., Weinberger A. J., Roberge A., Schneider G., 2013, ApJ, 771, 45
Dong R., Rafikov R. R., Stone J. M., 2011, ApJ, 741, 57
Duffell P. C., MacFadyen A. I., 2013, ApJ, 769, 41
Fu W., Li H., Lubow S., Li S., 2014, ApJ, 788, L41
Fukagawa M. et al., 2013, PASJ, 65, L14
Fung J., Shi J.-M., Chiang E., 2014, ApJ, 782, 88
Inaba S., Barge P., 2006, ApJ, 649, 415
Isella A., Pérez L. M., Carpenter J. M., Ricci L., Andrews S., Rosenfeld K., 2013, ApJ, 775, 30
Koller J., Li H., Lin D. N. C., 2003, ApJ, 596, L91
Lesur G., Papaloizou J. C. B., 2009, A&A, 498, L1
Li H., Finn J. M., Lovelace R. V. E., Colgate S. A., 2000, ApJ, 533, 1023
Li H., Colgate S. A., Wendroff B., Liska R., 2001, ApJ, 551, 874
Li H., Li S., Koller J., Wendroff B. B., Liska R., Orban C. M., Liang E. P. T., Lin D. N. C., 2005, ApJ, 624, 1003
Li H., Lubow S. H., Li S., Lin D. N. C., 2009, ApJ, 690, L52
Lin M.-K., 2012, ApJ, 754, 21
Lin M.-K., 2013, ApJ, 765, 84
Lin M.-K., Papaloizou J. C. B., 2010, MNRAS, 405, 1473
Lin M.-K., Papaloizou J. C. B., 2011, MNRAS, 415, 1426
Lovelace R. V. E., Hohlfeld R. G., 2013, MNRAS, 429, 529
Lovelace R. V. E., Li H., Colgate S. A., Nelson A. F., 1999, ApJ, 513, 805
Lyra W., Lin M.-K., 2013, ApJ, 775, 17
Lyra W., Johansen A., Klahr H., Piskunov N., 2009, A&A, 493, 1125
Masset F., 2000, A&AS, 141, 165
Meheut H., Lovelace R. V. E., Lai D., 2013, MNRAS, 430, 1988
Osorio M. et al., 2014, ApJ, 791, L36
Ou S., Ji J., Liu L., Peng X., 2007, ApJ, 667, 1220
Paardekooper S., Lesur G., Papaloizou J. C. B., 2010, ApJ, 725, 146
Papaloizou J., Lin D. N. C., 1984, ApJ, 285, 818
Pérez L. M., Isella A., Carpenter J. M., Chandler C. J., 2014, ApJ, 783, L13
Pinilla P., de Juan Ovelar M., Ataiee S., Benisty M., Birnstiel T., van Dishoeck E. F., Min M., 2015, A&A, 573, A9

Quanz S. P., Amara A., Meyer M. R., Kenworthy M. A., Kasper M., Girard J. H., 2013a, ApJ, 766, L1
Quanz S. P., Avenhaus H., Buenzli E., Garufi A., Schmid H. M., Wolf S., 2013b, ApJ, 766, L2
Railton A. D., Papaloizou J. C. B., 2014, MNRAS, 445, 4409
Reggiani M. et al., 2014, ApJ, 792, L23
Stone J. M., Norman M. L., 1992, ApJS, 80, 753
van der Marel N. et al., 2013, Science, 340, 1199
Yu C., Li H., Li S., Lubow S. H., Lin D. N. C., 2010, ApJ, 712, 198
Zhu Z., Stone J. M., Rafikov R. R., Bai X.-n., 2014, ApJ, 785, 122

This paper has been typeset from a TEX/LATEX file prepared by the author.